Habitats in DCE-MRI to Predict Clinically Significant Prostate Cancers

Nestor Andres Parra[1], Hong Lu[1,2], Jung Choi[3], Kenneth Gage[3], Julio Pow-Sang[4], Robert J. Gillies[1,3], and Yoganand Balagurunathan[1]

Departments of [1]Cancer Physiology, [3]Radiology, and [4]Urology, H.L. Moffitt Cancer Center, Tampa, FL; and [2]Department of Radiology, Tianjin Medical University Cancer Institute and Hospital, Tianjin, China

Corresponding Author:
Yoganand Balagurunathan, PhD
Cancer Physiology, H.L. Moffitt Cancer Center,
12902 USF Magnolia Ave, Tampa, FL 33612;
E-mail: Yoganand.Balagurunathan@moffitt.org.

Key Words: MRI, prostate cancer, machine learning, radiomics, habitats, DCE
Abbreviations: Dynamic contrast-enhanced imaging (DCE), prostatic-specific antigen, multiparametric magnetic resonance imaging (mpMRI), transrectal ultrasonography (TRUS), T2-weighted (T2W), diffusion-weighted imaging (DWI), peripheral zone (PZ), repetition time (TR), echo time (TE), endorectal coil (ERC), support vector machines (SVMs), regions of interest (ROIs), Area Under the Receiver Operating Characteristic curve (AUC), Non-negative matrix factorization (NMF)

Prostate cancer identification and assessment of clinical significance continues to be a challenge. Routine multiparametric magnetic resonance imaging has shown to be useful in assessing disease progression. Although dynamic contrast-enhanced imaging (DCE) has the ability to characterize perfusion across time and has shown enormous utility, radiological assessment (Prostate Imaging-Reporting and Data System or PIRADS version 2) has limited its use owing to lack of consistency and nonquantitative nature. In our work, we propose a systematic methodology to quantify perfusion dynamics for the DCE imaging. Using these metrics, *7 different subregions* or *perfusion habitats* of the targeted lesions are localized and related to clinical significance. We found that quantitative features describing the habitat based on the late area under the DCE time-activity curve was a good predictor of clinical significance disease. The best predictive feature in the habitat had an AUC of 0.82, CI [0.81–0.83].

INTRODUCTION

Prostate cancer is the second leading cause of cancer deaths among men in the United States and accounts to be the third largest among newly diagnosed cancer cases (19%) (1). Rising prostatic-specific antigen and abnormal digital-rectal examination have been traditionally used in the diagnosis of prostate cancer. Advent of improved imaging resulted in the inclusion of multiparametric magnetic resonance imaging (mpMRI) in the clinical workflow (2). Recently, the United States Preventive Services Task Force (USPSTF) has recommended against the routine use of prostatic-specific antigen testing for diagnosis of prostate cancer, owing to the risk of overdiagnosis and overtreatment (3, 4). Advancements in image acquisition and resolution of mpMRI coupled with the use of fusion-based transrectal ultrasonography (TRUS)– guided biopsy has improved disease detection and shown promise in improving diagnosis and treatment (5). Routine MP-MRI includes T2-weighted (T2W) imaging that describes the prostate anatomy, diffusion-weighted imaging (DWI) that measures the density of cellular space by quantifying the diffusion of water molecules. DCE image data shows the dynamics of the administered contrast agent, which characterizes the blood flow into prostate tissue and allows the identification of suspicious lesions by localizing abnormal contrast absorption.

DCE analysis can be quantitative or semiquantitative. The first approach is based on a contrast concentration model used to determine the rate of contrast transfer from the blood plasma into the tissue's extravascular extracellular space (6, 7). The second approach describes different contrast absorption patterns based on the characteristics of time–activity curves (8-10). The Prostate Imaging-Reporting and Data System (PI-RADSv2) currently includes DCE along with T2W and DWI, but their added value in diagnosis seems to be limited (11). PI-RADSv2 limits the use of DCE to the peripheral zone (PZ) when DWI is not conclusive. The standard limits the use of DCE to a single binary observation: presence or absence of uptake. This could be attributed to the lack of consensus in the community to use better metrics. Traditionally, these DCE curves are qualitatively characterized, which includes wash-in and wash-out slopes and time-to-peak (12). These have been related to tumor aggressiveness (13). The difficulty in establishing consistent features from the DCE curves, as well as the high interobserver variability, has limited the use of DCE in a quantitative fashion. Nonetheless, there have been successful efforts to semiquantitatively characterize DCE and use these parameters for classification of prostate cancer aggressiveness (14, 15).

Recently, radiomic analysis of habitats defined by textural kinetic features has been used to predict recurrence-free survival in patients with breast cancer (16). DCE-based habitats have shown to correlate with estrogen receptor and nodal metastatic status in breast cancer. Habitats in MRI imaging have also been useful in identifying disease progression in glioblastoma (17).
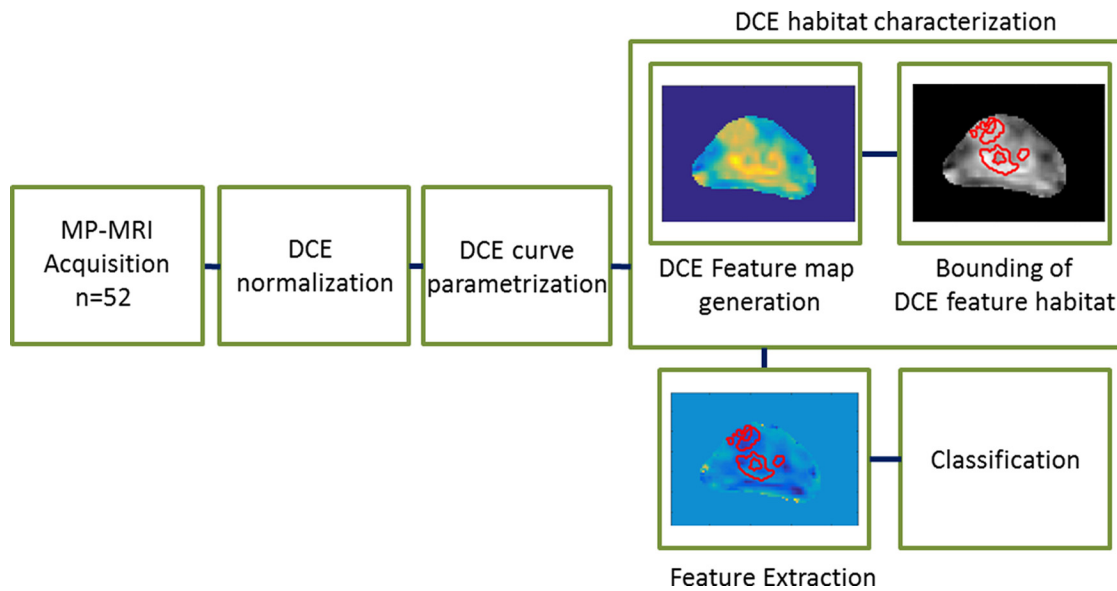
Figure 1. Block diagram shows the DCE habitat identification and processing. A perfusion tumor habitat was localized for each DCE feature map and these regions were characterized (by DCE features). Classification models were applied to identify features that can discriminate clinically significant prostate cancers.

MRI-defined features have been used to define radiotherapy treatment planning in prostate cancer (18).

In this study, we obtained the tumor region based on radiologist delineation on a T2W sequence. The region was centered on the TRUS biopsy location that was imported directly from the fused TRUS/MRI system. DCE characteristics at voxel level, across time, were quantified. Each feature map was used to form a habitat or localization of voxels. These new habitat regions were limited by a boundary around the known biopsy location that was quantified. The ability of the features to discriminate clinically significant cancers was evaluated for these specific habitats. Figure 1 shows the methodology followed.

METHODS
Patients and MRI Acquisition
Patient imaging and histopathology records were collected at H. Lee Moffitt Cancer Center, retrospective investigatory protocol approved by the University of South Florida IRB. Informed consent was waived for retrospective access of deidentified patient records. The study included patients that had MRI-guided targeted biopsy acquired between November 2015 and February 2018. Suspicious lesions were marked by a clinical radiologist on MRI. The patients in the study cohort had at least one biopsy with an assigned Gleason Score (GS) sum $\geq$6. The data set consisted of 72 biopsies from 54 patients. The average interval between imaging and biopsy sampling was 27 days. In this study, patients were grouped in 2 categories: *clinically insignificant cancer* (GS = 6) and *clinically significant cancer* (GS $\geq$ 7). All statistics were performed using this grouping. The data set consisted of 25 clinically insignificant and 47 clinically significant biopsies.

MRI Acquisition and DCE Normalization
Routine clinical MP-MRI acquisition includes T2-weighted imaging (T2W), DCE, and DWI. The DWI includes an apparent diffusion coefficient (ADC) map generated at the time of acquisition. Patients were injected with contrast agent Gadavist (Bayer HealthCare, Whippany, NJ) with a dose of 0.1 mL/kg before MRI-DCE acquisition. In total, 27 patients were imaged using a Siemens –SymphonyTim (Siemens, Munich, Germany) scanner at 1.5 T and endorectal coil (ERC) (eCoil, Medrad, Pittsburgh, PA) with median repetition time (TR) of 7.7 seconds (range, 6.4–9.5 seconds) and median echo time (TE) of 95 milliseconds (range, 94–95 milliseconds) for DWI. For DCE, TR was 4.72 milliseconds, TE was 1.34 milliseconds, flip angle was 12°, and temporal resolution was 11.45 seconds. Twenty-two patients were imaged using a Siemens-Skyra (Siemens, Munich, Germany) scanner at 3 T and a pelvic phased-array coil with a median TR of 4.6 seconds (range, 4.5–5.8 seconds) and a median TE of 77 milliseconds (range, 67–84 milliseconds) for DWI. For DCE, the median TR was 4.5 milliseconds (range, 4.5–5.08 milliseconds), the median TE was 1.71 milliseconds (range 1.71-1.87 milliseconds), flip angle was 12° (n = 20), and 15° (n = 2); temporal resolution was 11.45 seconds (n = 20) and 13.75 seconds (n = 2). Three patients were imaged on a Philips-Ingenia scanner at 3 T and a pelvic phased-array coil with a median TR of 6.0 seconds (range, 4.5– 6.2 seconds) and a median TE of 114 milliseconds (range, 91–114 milliseconds) for DWI. For DCE, the median TR was 4.21 milliseconds (range, 3.56–4.28 milliseconds), the median TE was 2.02 milliseconds (range, 1.62–2.08 milliseconds), flip angle was 10°, and temporal resolution was 13.75 seconds. In summary, 27 patients (38 biopsies, 14 clinically insignificant and 24 clinically signifi-

Table 1. Patients Enrolled in the Study With Their Biopsies Clinical Status and Scanner Differences

	Patients	Biopsies	Clinically Insignificant	Clinically Significant
1.5 T/ERC	27	38	14	24
3 T	25	34	11	23
Total	52	72	25	47

cant) were imaged at 1.5 T with ERC and 25 patients (34 biopsies, 11 clinically insignificant and 23 clinically significant) at 3 T with a phased-array pelvic coil (Table 1).

Image registration against the T2W image was performed for all modalities using gradient descent of mutual information on the space spanned by 3D affine transformations. Manual contours of the prostate, PZ, and the radiologist finding in the prebiopsy MRI were stored as RT-DICOM structures. The peak-absorption time point S_{peak} was identified in DCE using the AIF (arterial input function) signal as reference. All other time points were registered to S_{peak}. DCE data were normalized using an automatically segmented arterial contour as described in the literature (19), which makes the signal proportional to the change in relaxation rate caused by the contrast agent weighted by the initial spin-lattice relaxation time (20).

DCE-Feature Maps

Seven features were extracted from the DCE time–activity curves, which describe both early and late enhancement (Table 2). DCE time–activity curves were represented using a biexponential semiquantitative model (12) that has the following 5 parameters: initial static intensity s_O, plateau s_m, start of enhancement t_O, time-to-peak tau, and wash-out slope, wo. The online Supplemental Figure 1 shows an example with the parameters used to characterize the DCE time activity curve. Peak enhancement $s_p = s_m - s_O$, wash-in slope $wi = s_p/tau$. In addition, we computed 2 features that describe the area under the DCE curve between a time interval, namely: AUC_{t1-t2} is the area under the biexponential fitted DCE curve between time t1 and t2. $AUCi = AUC_{t0-t0+60}$ measures the early wash-in uptake curve and $AUCf = AUC_{t0+240-t0+270}$ measures the late wash-

out curve. The seventh feature computes the multiplicative effect of wash-in and wash-out slopes and was computed as $m_{io} = wi * wo$. Each one of these parameters was used to generate a 3D DCE-feature map that was used to obtain a habitat (Figure 2).

Habitat Representation

We localized the regions of interest (ROIs) based on each of the 7 DCE feature maps, which includes intra and peritumoral regions around the biopsy location, referred to as *DCE based Habitats*. A sphere (radius $r = 15$ mm) around the biopsy location was placed on each DCE feature map used to bound the tumor habitat. This region was additionally bounded by the prostate zones (PZ or peripheral zone, TZ or transitional zone) allowing convergence of largest lesion volume. The values for each feature map within the localized sphere were used to obtain the region defined by either the lower or upper quartile depending on the feature. The converged habitats were labeled as *H-DCE feature*. The mean DCE signal at the converged habitat region at each sampling time was used as a representative perfusion curve for the patient biopsy. DICE index between each habitat and the radiologist's lesion ROI were computed to assess the volume of intratumoral habitat.

Statistical Analysis

Univariate analysis of the 7 DCE features was performed to evaluate the overall discrimination using support vector machines (SVMs) to discriminate clinically significant cancers. Sensitivity, specificity, and AUC were computed on the habitats (Table 3). Pair-wise multivariable analysis was performed by exhaustive comparison of all possible DCE features. The under-represented GS class was oversampled using SMOTE (21), cali-

Table 2. List of DCE Features

Number	Feature ID	Feature Description	Dice
1	s_P	Peak enhancement, s_m-s_O	0.22
2	tau	Time-to-peak	0.42
3	wi	Wash-in slope	0.21
4	wo	Wash-out slope	0.25
5	$AUCi$	Initial AUC, $AUC_{t0-t0+60}$	0.33
6	$AUCf$	Final (late) AUC, $AUC_{t0+240-t0+270}$	0.22
7	m_{io}	Slope product, $wi \times wo$	0.17

The DCE features were used in this paper to converge a *habitat* from the associated feature map and to characterize the average time activity curve in each *habitat*.
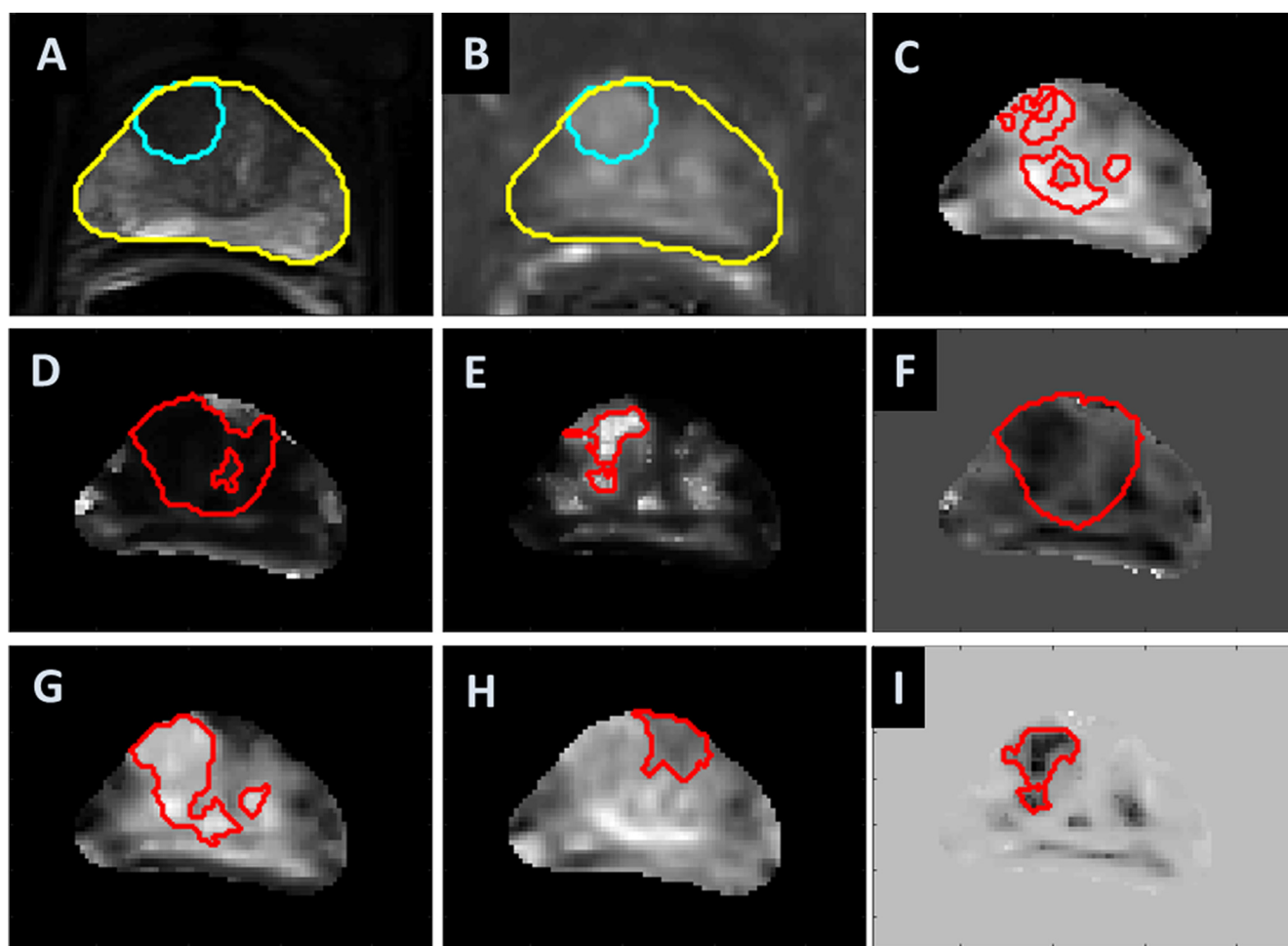
Figure 2. Example of prostate habitats based on DCE features. Radiologist's outline of an anterior lesion in the transition zone (TZ) (cyan) and prostate (yellow) contours overlapped with T2-weighted (T2w) imaging (A) and peak-enhancement DCE series (B). DCE feature maps for peak enhancement (C), time-to-peak (D), wash-in slope (E), wash-out slope (F), early AUC (G), late AUC (H), and slope product (I). DCE feature maps were built by parametrizing the DCE features for every voxel in the prostate.

brated so that both classes had matched sample size. Classifier performance was evaluated using *leave-1-out* cross-validation. Each classification experiment was repeated 50 times. Further, 95% confidence intervals for sensitivity, specificity, and AUC were estimated. Image processing and segmentations were performed on commercial imaging Picture Archive Communication System (PACS) workstation (MIM Corporation, Cleveland, OH, USA). Classifiers and feature computations were developed using custom code written in C++ and Matlab.

RESULTS

In this study we evaluated the predictive performance of *DCE (perfusion) habitats*, confined regions with similar perfusion behavior in the intra and peritumoral regions, using established characteristics of the DCE time activity curves. We determined a set of 7 parameters from a biexponential curve fitting of these curves (see online Supplemental Figure 1). These parameters generate feature maps (Figure 2) that were used to generate 1 habitat for each

identified lesion. DICE score between habitats and manual lesion contours ranged between 0.17 and 0.42 (Table 2).

The discriminatory ability of each feature was evaluated performing univariate classification using SVM, repeated for each habitat (Table 3 and online Supplemental Table 1). The top performing habitat was the *slope product* habitat ($H\text{-}m_{io}$), with AUC for its DCE features in the range 0.46–0.78. The best predictive features were *tau* (AUC, 0.71 [0.69, 0.73]; sensitivity, 0.66 [0.64, 0.69]), followed by *wo* (AUC, 0.74 [0.73, 0.75]; sensitivity, 0.62 [0.60, 0.64]) and m_{io} (AUC, 0.78 [0.77, 0.79]; sensitivity, 0.68 [0.68, 0.68]).

Additionally, we separated the samples for consistent scanner types. For 1.5 T/ERC, the top performing habitats were the *late AUC* habitat ($H\text{-}AUCf$) and $H\text{-}m_{io}$ (Table 4 and online Supplemental Table 2). For $H\text{-}AUCf$, the best predictive feature was *wi* (AUC, 0.81 [0.80, 0.82]; sensitivity, 0.74 [0.72, 0.75]), and for $H\text{-}m_{io}$, the best predictive feature was s_p (AUC, 0.78 [0.76, 0.80]; sensitivity, 0.79 [0.76, 0.81]). For 3 T, the top performing habitats were $H\text{-}AUCf$ and the *peak enhancement* habitat ($H\text{-}s_p$)

Table 3. Univariate Evaluation of DCE-Based Habitats Versus DCE Features

	Feature						
	s_P	tau	wi	wo	AUCi	AUCf	m_{io}
Habitat							
H-s_P							
Sensitivity	0.54	0.76	0.60	0.68	0.43	0.56	0.64
Specificity	0.58	0.66	0.69	0.52	0.50	0.53	0.63
AUC	0.56	0.71	0.65	0.60	0.47	0.54	0.63
H-tau							
Sensitivity	0.44	0.55	0.71	0.59	0.49	0.71	0.71
Specificity	0.37	0.54	0.61	0.52	0.53	0.62	0.46
AUC	0.41	0.55	0.66	0.55	0.51	0.67	0.58
H-wi							
Sensitivity	0.48	0.40	0.54	0.51	0.58	0.58	0.44
Specificity	0.49	0.55	0.52	0.45	0.54	0.49	0.53
AUC	0.48	0.48	0.53	0.48	0.56	0.53	0.49
H-wo							
Sensitivity	0.55	0.71	0.60	0.65	0.59	0.56	0.58
Specificity	0.48	0.57	0.62	0.70	0.55	0.50	0.70
AUC	0.52	0.64	0.61	0.67	0.57	0.53	0.64
H-AUCi							
Sensitivity	0.57	0.49	0.47	0.59	0.55	0.55	0.55
Specificity	0.48	0.63	0.45	0.46	0.52	0.59	0.45
AUC	0.53	0.56	0.46	0.52	0.53	0.57	0.50
H-AUCf							
Sensitivity	0.55	0.68	0.66	0.63	0.68	0.57	0.71
Specificity	0.68	0.74	0.49	0.51	0.58	0.52	0.57
AUC	0.62	0.71	0.58	0.57	0.63	0.54	0.64
H-m_{io}							
Sensitivity	0.65	0.66	0.42	0.62	0.45	0.57	0.68
Specificity	0.57	0.75	0.69	0.86	0.46	0.41	0.88
AUC	0.61	0.71	0.56	0.74	0.46	0.49	0.78

Seven habitats were outlined by thresholding DCE feature maps (columns). For each habitat, the mean DCE feature values were computed (rows). Mean sensitivity, mean specificity, and mean AUC for classification between clinically insignificant and clinically significant cancer, based on MRI-guided biopsies. SVMs were used as classifiers with leave-1-out cross-validation. All patients in the study were included.

(Table 5 and online Supplemental Table 3). For the habitat based on the late area under the DCE time–activity curve (*H-AUCf*), the best predictive feature was *tau* (AUC, 0.83 [0.82, 0.85]; sensitivity, 0.69 [0.69, 0.70]), and for the *H-s_P*, the best predictive feature was *wo* (AUC, 0.81 [0.80, 0.83]; sensitivity, 0.85 [0.83, 0.86]).

The late AUC habitat (*H-AUCf*) was selected for pair-wise feature analysis because it had shown accurate features for both cohorts being robust for scanner strength/acquisition coil. Pair-wise analysis of this habitat showed that 2 pairs of features were predictive in both the 1.5/ERC data set and the 3 T data set. These pairs were (*tau*, *wi*) and (*wo*, *AUCi*) (Table 6 and online Supplemental Tables 4 and 5). Classification using the feature pair (*tau*, *wi*) had an AUC of 0.80 [0.79, 0.81] and a sensitivity 0.71 [0.70, 0.72] for 1.5 T and an AUC of 0.84 [0.83, 0.85] and a sensitivity

0.76 [0.75, 0.77] for 3 T. Classification using the feature pair (*wo*, *AUCi*) had an AUC of 0.82 [0.81, 0.83] and a sensitivity 0.80 [0.79, 0.81] for 1.5 T and an AUC of 0.81 [0.80, 0.82] and a sensitivity 0.73 [0.72, 0.75] for 3 T.

DISCUSSION

In our current work we present an approach to converge on a region (habitat) and quantify its DCE (perfusion) characteristics to discriminate clinically aggressive cancers. Prior work on perfusion characterization has shown DCE values extracted from ROIs correlates with pathological assessment (GS), using intra-subject nonlinear matrix factorization to identify a suspicious region (10). Owing to varied scanner types, using direct voxel intensity values, coupled with the nondeterministic nature of non-negative matrix factorization, limits the ability of the

Table 4. Univariate Evaluation of 1.5 T ERC DCE-Based Habitats Versus DCE Features

1.5 T ERC	Feature						
	s_p	tau	wi	wo	AUCi	AUCf	m_{io}
Habitat							
$H\text{-}s_p$							
Sensitivity	0.54	0.63	0.58	0.7	0.58	0.51	0.52
Specificity	0.45	0.7	0.67	0.53	0.59	0.5	0.42
AUC	0.49	0.66	0.63	0.62	0.59	0.5	0.47
$H\text{-}tau$							
Sensitivity	0.47	0.6	0.64	0.72	0.5	0.53	0.62
Specificity	0.45	0.53	0.68	0.53	0.55	0.52	0.49
AUC	0.46	0.57	0.66	0.62	0.53	0.52	0.56
$H\text{-}wi$							
Sensitivity	0.39	0.56	0.6	0.52	0.49	0.51	0.47
Specificity	0.53	0.59	0.43	0.63	0.54	0.51	0.44
AUC	0.46	0.57	0.52	0.57	0.52	0.51	0.46
$H\text{-}wo$							
Sensitivity	0.42	0.59	0.67	0.43	0.55	0.57	0.57
Specificity	0.65	0.51	0.6	0.49	0.58	0.42	0.52
AUC	0.54	0.55	0.64	0.46	0.57	0.49	0.54
$H\text{-}AUCi$							
Sensitivity	0.43	0.71	0.64	0.52	0.51	0.37	0.59
Specificity	0.55	0.69	0.52	0.64	0.43	0.45	0.55
AUC	0.49	0.7	0.58	0.58	0.47	0.41	0.57
$H\text{-}AUCf$							
Sensitivity	0.42	0.55	**0.74**	0.46	0.72	0.56	0.65
Specificity	0.42	0.74	**0.88**	0.48	0.76	0.64	0.66
AUC	0.42	0.64	**0.81**	0.47	0.74	0.6	0.66
$H\text{-}m_{io}$							
Sensitivity	**0.79**	0.65	0.61	0.66	0.72	0.72	0.63
Specificity	**0.78**	0.63	0.81	0.59	0.79	0.66	0.46
AUC	**0.78**	0.64	0.71	0.62	0.75	0.69	0.55

Seven habitats were outlined by thresholding DCE feature maps (columns). For each habitat, the mean DCE feature values were computed (rows). Mean sensitivity, mean specificity, and mean AUC for classification between clinically insignificant and clinically significant cancer, based on MRI-guided biopsies. SVMs were used as classifiers with leave-1-out cross-validation. All patients in the study were included. The two features with the largest AUC amongst all habitats have been indicated in boldface.

method to reproduce across varied cohorts. The habitat model presented here addresses the key issue of showing a means to localize the ROI before quantification. We use SVM classifiers to discern the habitat and quantified features on this habitat that improved the ability to discriminate aggressive cancers (22).

The use of parameters from pharmacokinetics modeling has shown to lack robustness. A recent study has shown usability of Ktrans map to localize the tumor region and these maps have been reported to be predictive of tumor aggressiveness (13). It has also been reported that repeatability of Ktrans maps across institutions has been low, and a recent report shows a coefficient of variation to be as high as 0.59 (23).

There is an open debate about the accuracy of ERC and pelvic phased-array coil for the detection of prostate cancer. At

1.5 T, ERC produces a higher-quality imaging of the prostate with common artifacts in the PZ. At 3 T, the pelvic phased-array coil produces high-quality images without the inconvenience and cost of an ERC. Because both of these technologies are currently used in the clinic, we strive to find DCE features that are robust to both acquisition coil and magnetic field strength of the scanner. It is imperative to develop prognostic features that work well with both types of coils. In this paper we review the robustness of DCE features in the prediction of clinically aggressive cancers, with respect to the acquisition settings.

To improve the accuracy and reproducibility of classifications, the patients were divided according to the MRI acquisition characteristics, and their habitats were analyzed separately, identifying DCE features that were common in both subsets. The *late AUC*

Table 5. Univariate Evaluation of 3 T Pelvic Coil DCE-Based Habitats Versus DCE Features

3 T PELVIC	Feature						
	s_p	tau	wi	wo	AUCi	AUCf	m_{io}
Habitat							
H-s_p							
Sensitivity	0.52	0.59	0.6	**0.85**	0.7	0.65	0.67
Specificity	0.62	0.8	0.89	**0.78**	0.54	0.71	0.79
AUC	0.57	0.7	0.74	**0.81**	0.62	0.68	0.73
H-tau							
Sensitivity	0.67	0.49	0.64	0.58	0.4	0.68	0.69
Specificity	0.69	0.66	0.6	0.56	0.61	0.79	0.58
AUC	0.68	0.57	0.62	0.57	0.51	0.73	0.63
H-wi							
Sensitivity	0.78	0.31	0.54	0.51	0.68	0.59	0.57
Specificity	0.68	0.64	0.57	0.46	0.57	0.69	0.57
AUC	0.73	0.48	0.55	0.48	0.63	0.64	0.57
H-wo							
Sensitivity	0.66	0.46	0.45	0.56	0.45	0.72	0.5
Specificity	0.56	0.36	0.47	0.67	0.48	0.52	0.61
AUC	0.61	0.41	0.46	0.61	0.46	0.62	0.56
H-AUCi							
Sensitivity	0.54	0.5	0.56	0.58	0.58	0.69	0.7
Specificity	0.63	0.6	0.55	0.67	0.62	0.8	0.6
AUC	0.59	0.55	0.55	0.63	0.6	0.75	0.65
H-AUCf							
Sensitivity	0.66	**0.69**	0.64	0.53	0.56	0.66	0.58
Specificity	0.62	**0.97**	0.68	0.87	0.65	0.64	0.89
AUC	0.64	**0.83**	0.66	0.7	0.6	0.65	0.73
H-m_{io}							
Sensitivity	0.68	0.59	0.51	0.47	0.55	0.48	0.52
Specificity	0.53	0.61	0.58	0.66	0.52	0.39	0.69
AUC	0.6	0.6	0.54	0.57	0.54	0.44	0.61

Seven habitats were outlined by thresholding DCE feature maps (columns). For each habitat, the mean DCE feature values were computed (rows). Mean sensitivity, mean specificity, and mean AUC for classification between clinically insignificant and clinically significant cancer, based on MRI-guided biopsies. SVMs were used as classifiers with leave-1-out cross-validation. All patients in the study were included. The two features with the largest AUC amongst all habitats have been indicated in boldface.

habitat (*H-AUCf*) showed good performance (with features having an AUC greater than 0.8) for both scanner settings. The *peak enhancement* habitat (*H-s_p*) in the 3 T data set had the largest sensitivity with the *wo* feature (AUC, 0.81 [0.80, 0.83]; sensitivity, 0.85 [0.83, 0.86]) but failed to be robust with the 1.5 T/ERC cohort (AUC, 0.62 [0.60, 0.64]; sensitivity, 0.70 [0.68, 0.72]).

Further pair-wise analysis of the *H-AUCf* habitat showed improvement for classification accuracy. For 3 T, 10 pairs of features showed AUC larger or equal to 0.8, while for 1.5 T/ERC, there were only 3 pairs. This may suggest that 3 T acquisition provides better predictive features on DCE images compared to 1.5 T with endorectal coil. The *H-AUCf* habitat had a DICE score of 0.22, suggesting that this habitat was mostly exploring the peritumoral region, adding information to the model from the

surrounding environment. Two DCE feature pairs performed well: (*tau, wi*) and (*wo, AUCi*). The (*wo, AUCi*) pair had a sensitivity of 0.80 for 1.5 T/ERC and the (*tau, wi*) pair had a sensitivity of 0.76 for 3 T. Because we are aiming for features with high accuracy and high sensitivity, future experiments should evaluate if the tuple (*wo, AUCi, tau, wi*) would provide robust accuracy with high sensitivity. The main limitation of this study is the small sample size used for training; we expect using a conservative approach such as ours, would have a better chance of reproducibility.

CONCLUSION

We present a systematic quantitative methodology to identify DCE perfusion regions that provide quantitative assessment of DCE characteristics in these regions. We show that these metrics identify

Table 6. Evaluation of pairs of DCE features for habitat *H-AUCf*

	1.5 T ERC							3 T						
	s_P	tau	wi	wo	AUCi	AUCf	m_{io}	s_P	tau	wi	wo	AUCi	AUCf	m_{io}
Sensitivity														
s_P	0.42	0.74	0.64	0.75	0.70	0.60	0.64	0.66	0.76	0.61	0.70	0.74	0.65	0.74
tau		0.55	**0.71**	0.76	0.76	0.72	0.70		0.69	**0.76**	0.75	0.70	0.70	0.68
wi			0.74	0.63	0.73	0.68	0.60			0.64	0.63	0.61	0.70	0.73
wo				0.46	**0.80**	0.69	0.72				0.53	**0.73**	0.75	0.69
AUCi					0.72	0.73	0.69					0.56	0.77	0.64
AUCf						0.56	0.63						0.66	0.74
m_{io}							0.65							0.58
Specificity														
s_P	0.42	0.91	0.89	0.75	0.77	0.56	0.62	0.62	0.82	0.81	0.91	0.83	0.77	0.97
tau		0.74	**0.89**	0.72	0.81	0.86	0.70		0.98	**0.93**	0.98	0.84	0.83	0.94
wi			0.88	0.77	0.84	0.87	0.84			0.68	0.93	0.85	0.82	0.95
wo				0.48	**0.84**	0.66	0.67				0.87	**0.88**	0.91	0.94
AUCi					0.76	0.79	0.84					0.65	0.83	0.93
AUCf						0.64	0.63						0.64	0.91
m_{io}							0.66							0.89
AUC														
s_P	0.42	0.83	0.76	0.75	0.74	0.58	0.63	0.64	0.79	0.71	0.80	0.79	0.71	0.85
tau		0.64	**0.80**	0.74	0.79	0.79	0.70		0.83	**0.84**	0.87	0.77	0.76	0.81
wi			0.81	0.70	0.78	0.78	0.72			0.66	0.78	0.73	0.76	0.84
wo				0.47	**0.82**	0.67	0.69				0.70	**0.81**	0.83	0.82
AUCi					0.74	0.76	0.76					0.60	0.80	0.79
AUCf						0.60	0.63						0.65	0.83
m_{io}							0.66							0.73

Sensitivity, specificity, and AUC for classification between clinically insignificant and significant cancer is shown, based on MRI-guided biopsies. Support vector machines were used as classifiers. Leave-1-out cross-validation was used. The diagonal corresponds to the univariate case. The two features with the largest average AUC between 1.5 T and 3 T acquisitions have been indicated in boldface.

clinically significant cancers. In particular, we find that habitat regions identified by the late area under the DCE time–activity curve (*H-AUCf*) yield features to be related to clinically significant cancers. We also find that using a cohesive cohort with higher magnetic field strength (3 T) seems to improve the predictor performance.

Supplemental Materials

Supplemental Figure 1: http://dx.doi.org/10.18383/j.tom.2018.00037.sup.01

Supplemental Tables 1-5: http://dx.doi.org/10.18383/j.tom.2018.00037.sup.02

REFERENCES

1. Siegel RL, Miller KD, Jemal A. Cancer statistics, 2016. CA Cancer J Clin. 2016; 66:7–30.
2. Dianat SS, Carter HB, Macura KJ. Performance of multiparametric magnetic resonance imaging in the evaluation and management of clinically low-risk prostate cancer. Urol Oncol. 2014;32:39.e1–39.e10.
3. Lin K, Lipsitz R, Janakiraman S. Benefits and Harms of Prostate-Specific Antigen Screening for Prostate Cancer: An Evidence Update for the U.S. Preventive Services Task Force. Ann Intern Med. 2008;149:192–199.
4. Akizhanova M, Iskakova EE, Kim V, Wang X, Kogay R, Turebayeva A, Sun Q, Zheng T, Wu S, Miao L, Xie Y. PSA and Prostate Health Index based prostate cancer screening in a hereditary migration complicated population: implications in precision diagnosis. J Cancer. 2017;8:1223–1228.
5. Harvey CJ, Pilcher J, Richenberg J, Patel U, Frauscher F. Applications of transrectal ultrasound in prostate cancer. Br J Radiol. 2012;85 Spec Iss 1:S3–S17.

6. Tofts PS, Kermode AG. Measurement of the blood-brain barrier permeability and leakage space using dynamic MR imaging. 1. Fundamental concepts. Magn Reson Med. 1991;17:357–367.

7. Vajuvalli NN, Chikkemenahally DK, Nayak KN, Bhosale MG, Geethanath S. The Tofts model in frequency domain: fast and robust determination of pharmacokinetic maps for dynamic contrast enhancement MRI. Phys Med Biol. 2016;61:8462–8475.

8. Vos EK, Kobus T, Litjens GJ, Hambrock T, Hulsbergen-van de Kaa CA, Barentsz JO, Maas MC, Scheenen TW. Multiparametric magnetic resonance imaging for discriminating low-grade from high-grade prostate cancer. Invest Radiol. 2015;50:490–497.

9. Ginsburg SB, Algohary A, Pahwa S, Gulani V, Ponsky L, Aronen HJ, Boström PJ, Böhm M, Haynes AM, Brenner P, Delprado W, Thompson J, Pulbrock M, Taimen P, Villani R, Stricker P, Rastinehad AR, Jambor I, Madabhushi A. Radiomic features for prostate cancer detection on MRI differ between the transition and peripheral zones: Preliminary findings from a multi-institutional study. J Magn Reson Imaging. 2017;46:184–193.

10. Parra NA, Pollack A, Chinea FM, Abramowitz MC, Marples B, Munera F, Castillo R, Kryvenko ON, Punnen S, Stoyanova R. Automatic detection and quantitative DCE-MRI scoring of prostate cancer aggressiveness. Front Oncol. 2017;7:259.

11. American College of Radiology. Prostate Imaging Reporting and Data System (PIRADS) version 2. 2015. https://www.acr.org/~/media/ACR/Documents/PDF/QualitySafety/Resources/PIRADS/PIRADS%20V2.pdf.

12. Huisman HJ, Engelbrecht MR, Barentsz JO. Accurate estimation of pharmacokinetic contrast-enhanced dynamic MRI parameters of the prostate. J Magn Reson Imaging. 2001;13:607–614.

13. Vos EK, Litjens GJ, Kobus T, Hambrock T, Hulsbergen-van de Kaa CA, Barentsz JO, Huisman HJ, Scheenen TW. Assessment of prostate cancer aggressiveness using dynamic contrast-enhanced magnetic resonance imaging at 3 T. Eur Urol. 2013;64:448–455.

14. Litjens G, Debats O, Barentsz J, Karssemeijer N, Huisman H. Computer-aided detection of prostate cancer in MRI. IEEE Trans Med Imaging. 2014;33:1083–1092.

15. Chen YJ, Chu WC, Pu YS, Chueh SC, Shun CT, Tseng WY. Washout gradient in dynamic contrast-enhanced MRI is associated with tumor aggressiveness of prostate cancer. J Magn Reson Imaging. 2012;36:912–919.

16. Wu J, Cao G, Sun X, Lee J, Rubin DL, Napel S, Kurian AW, Daniel BL, Li R. Intratumoral spatial heterogeneity at perfusion MR imaging predicts recurrence-free survival in locally advanced breast cancer treated with neoadjuvant chemotherapy. Radiology. 2018;288:26–35.

17. Lee J, Narang S, Martinez J, Rao G, Rao A. Spatial habitat features derived from multiparametric magnetic resonance imaging data are associated with molecular subtype and 12-month survival status in glioblastoma multiforme. PLoS One. 2015;10:e0136557.

18. Stoyanova R, Chinea F, Kwon D, Reis IM, Tschudi Y, Parra NA, Breto AL, Padgett KR, Pra AD, Abramowitz MC, Kryvenko ON, Punnen S, Pollack A. An automated multiparametric MRI quantitative imaging prostate habitat risk scoring system for defining external beam radiotherapy boost volumes. Int J Radiat Oncol Biol Phys. 2018;102:821–829.

19. Farjam R, Tsien CI, Lawrence TS, Cao Y. DCE-MRI defined subvolumes of a brain metastatic lesion by principle component analysis and fuzzy-c-means clustering for response assessment of radiation therapy. Med Phys. 2014;41:011708.

20. Haase A. Snapshot FLASH MRI. Applications to T1, T2, and chemical-shift imaging. Magn Reson Med. 1990;13:77–89.

21. Chawla NV, Bowyer KW, Hall LO, Kegelmeyer WP. SMOTE: synthetic minority over-sampling technique. J Artif Intell Res. 2002;16:321–357.

22. Cristianini N, Shawe-Taylor J. An Introduction to Support Vector Machines: And Other Kernel-based Learning Methods. Cambridge: Cambridge University Press. 2000.

23. Huang W, Li X, Chen Y, Li X, Chang MC, Oborski MJ, Malyarenko DI, Muzi M, Jajamovich GH, Fedorov A, Tudorica A, Gupta SN, Laymon CM, Marro KI, Dyvorne HA, Miller JV, Barbodiak DP, Chenevert TL, Yankeelov TE, Mountz JM, Kinahan PE, Kikinis R, Taouli B, Fennessy F, Kalpathy-Cramer J. Variations of dynamic contrast-enhanced magnetic resonance imaging in evaluation of breast cancer therapy response: a multicenter data analysis challenge. Transl Oncol. 2014;7:153–166.